IEEE Access
Multidisciplinary | Rapid Review | Open Access Journal

Received 15 January 2023, accepted 6 February 2023, date of publication 13 February 2023, date of current version 16 February 2023.

Digital Object Identifier 10.1109/ACCESS.2023.3244401

RESEARCH ARTICLE

Wideband 5G Antenna Gain Enhancement Using a Compact Single-Layer Millimeter Wave Metamaterial Lens

CHAKER MOHSEN SALEH[1,*], EQAB ALMAJALI[2,*], (Member, IEEE), ANWAR JARNDAL[2], (Senior Member, IEEE), JAWAD YOUSAF[3], SAQER S. ALJA'AFREH[4], AND RONY E. AMAYA[5], (Senior Member, IEEE)

[1]Department of Electronics, Telecommunications Signals and Systems Laboratory, University of Amar Telidji, Laghouat 03000, Algeria
[2]Electrical Engineering Department, University of Sharjah, Sharjah, United Arab Emirates
[3]Department of Electrical, Computer, and Biomedical Engineering, Abu Dhabi University, Abu Dhabi, United Arab Emirates
[4]Electrical Engineering Department, Mutah University, Mu'tah 61710, Jordan
[5]Department of Electronics, Carleton University, Ottawa, ON K1S 5B6, Canada

Corresponding author: Eqab Almajali (ealmajali@sharjah.ac.ae)

*Chaker Mohsen Saleh and Eqab Almajali contributed equally to this work.

ABSTRACT This paper presents a very compact, wideband, and enhanced-gain antenna for 5G applications. A simple single-layer millimeter wave (mm-wave) metamaterial lens (meta-lens) is used to improve the gain, aperture efficiency, and gain bandwidth of a slotted-patch antenna over a wide range of frequencies from 25 GHz to 31 GHz. The lens exhibits a metamaterial negative refractive index behavior, which is attributed to a substantial gain enhancement of around 4-5 dBi over the whole band compared to the gain values of the slotted patch antenna alone. The lens's unit cell comprises a simple single-layer split ring resonator (SRR) whose dimensions are carefully chosen to improve transmitted power and suppress absorbed and reflected power. The meta-lens consists of 8×8 subwavelength SRR unit cells. Each cell has an area of 1.6×1.6 mm^2, it is located in the near-field region closely above a slotted patch antenna to produce a total antenna size of $12.8 \times 12.8 \times 7.27$mm^3 ($1.2\ \lambda \times 1.2\ \lambda \times 0.68\ \lambda$, where λ is the free space wavelength at 28 GHz). The maximum gain of the proposed antenna is 12.7 dBi, the 1 dB gain bandwidth is 18%, the maximum aperture efficiency is 92%, and the -10 dB impedance bandwidth (10 dB B.W.) is 17%. This excellent combination of essential metrics is hard to realize at mm-wave using narrowband antenna structures (microstrip patch antennas), and the aperture efficiency is the highest thus far for such a class of antennas.

INDEX TERMS Wideband 5G antenna, gain enhancement, aperture efficiency, negative refractive index, millimeter wave meta-lens.

I. INTRODUCTION

Despite the mm-wave 5G bands, like the 28 GHz band, have been licensed by the Federal Communication Commission (FCC) and many other regulatory bodies across the world for years thus far [1], the existing technology (4G/WiFi/WLAN) is still using microwave sub-6 GHz bands. This delay in realizing a true high data rate system at mm-wave bands is caused by some challenges associated with the design and implementation of mm-wave systems and antennas [2]. For mm-wave 5G applications, antennas need to generally possess a high gain, wide bandwidth, diversity of polarization, and possibly a reconfigurable (agile) radiation pattern; while remaining very compact to fit into small packages [2], [3]. These characteristics are often inversely related; therefore, the structured artificial bi- and three-dimensional materials such as metamaterials and Electromagnetic/Photonic Bandgap Materials (E/PBG) can offer extra-ordinary solutions for these purposes [4], [5].

Among the metamaterial applications in the antenna field, antenna gain and bandwidth enhancements have been reported in [6], [7], [8]. In this regard, several works have introduced a superstrate of metamaterial/metasurface characteristics on top of a single radiating element to boost the

The associate editor coordinating the review of this manuscript and approving it for publication was Debabrata K. Karmokar.

overall antenna gain; while maintaining a small antenna footprint. This was mainly done to avoid the conventional way of achieving higher gain values by adding more radiating antenna elements hence, obtaining large aperture sizes. In [9], a single layer metamaterial superstrate comprises of 4×4 ring elements is placed on top of a diagonal radiating slot to improve its gain and operational bandwidth. The 10 dB B.W. achieved in [9] covers the entire licensed mm-wave range 24.2-29.5 GHz with an actual small footprint of $1.1\ \lambda\times1.1\ \lambda$ (at 27.5 GHz5GHz); however; the maximum achieved gain was only 11 dBi, which corresponds to an aperture efficiency of 82% for the antenna. Another exciting design reported in [10] has also utilized a single layer mm-wave FSS superstrate placed above a radiating dielectric resonator antenna (DRA) with an air gap of 0.5 λ in between. The 10 dB B.W. covers the frequency band from 26 GHz to 30.3 GHz with a maximum measured gain of 15.7 dBi. The large footprint of $2.9\ \lambda\times9\lambda\times\ 2.9\ \lambda$ of the superstrate in [10] has contributed to the gain improvement; however, this resulted in an aperture efficiency below 50% and the predicted 1 dB gain B.W. is only 4% (estimated from the gain versus frequency figure). A three-layer dual split ring mm-wave metamaterial lens is used in [4] to improve the gain of a magneto-electric dipole. The antenna in [4] supports circular polarization and has a wide 10 dB B.W. that spans from 29.5 GHz to 37 GHz; however, the maximum gain value achieved is 10.5 dBi. The design also utilizes multilayers and hence it requires advanced manufacturing facilities. A Substrate Integrated Waveguide (SIW) is used in [11] to excite a low-profile metasurface comprising of Maltese cross-shaped edge patches. Two frequency bands were covered efficiently namely, 23.7-29.2 GHz and 36.7-41.1 GHz however; the maximum gain values achieved are 7.4 dBi and 10.9 dBi in the lower and upper bands, respectively for an antenna footprint area of $2.8\ \lambda\times\ 1.5\ \lambda\ m^2$.

Metasurfaces have also been utilized at none mm-wave frequency bands for gain and bandwidth enhancement of a single radiating antenna element. Interesting examples of such works are reported in [12], [13], [14], and [15]. In [12], a metamaterial surface was used as a superstrate above a patch antenna designed at 10 GHz. The maximum gain achieved is 12.5 dBi; while the -10 dB fractional B.W. is below 10%. The footprint is around $2\lambda\times2\lambda$ at 10 GHz. In [13] a dual-layer meta-lens is used to increase the gain and 10 dB impedance B.W. of a Reactive Impedance Surface (RIS) backed patch antenna. The design band in [13] covers 6.5-8.5 GHz with a maximum reported gain of 13.9 dBi and a -10 dB fractional B.W. of 13% (7.2 – 8.2 GHz). The calculated 1 dB gain bandwidth from the available data in [13] is only 3%. Another dual-layer metasurface, reported in [14], is placed on top of an orthogonal shape aperture to improve its performance. It was designed to operate in the 4.5 – 7.5 GHz band with a maximum gain of 7 dBi and a fractional B.W. of 36% (5.04 – 7.21 GHz). A single-layer metamaterial lens is designed in [15] for LTE 46/WLAN applications in the 5-7 GHz band. The lens was placed on top of a truncated patch with a truncated ground plane. The maximum gain was 5.54 dBi with a 10 dB B.W. close to 7% (5.35-5.69 GHz).

Other techniques that were used to improve mm-wave single-element antenna gain; while maintaining a small footprint include Electromagnetic Band Gaps (EBGs) and Defected Groundplane (D.G.) [5], [16], [17]. The EBGs can be mainly used for gain improvement due to the known narrowband nature of resonant cavities [18]. In [16], a 2×2 printed Yagi structure was reinforced by an EBG structure with a suspended strip line to improve gain and fractional B.W. However, the structure is comprised of four layers designed to operate in the 25 -33 GHz band. Also, its footprint is quite large ($13\ \lambda\times13\ \lambda$), produced a maximum gain of 11.9 dBi, and has a fractional bandwidth of 17%. A patch with a defected ground plane was proposed in [17] for mm-wave applications (25-34 GHz). By using a D.G., a fractional bandwidth of 22% was achieved (26.5-32.9 GHz), however, the maximum reported gain value was as low as 5.6 dBi. Element shaping was also used to improve antenna gain and bandwidth characteristics at different frequency bands with less gain improvement than metamaterial lenses and EBGs. Examples of such works are reported in [19], [20], and [21].

For mm-wave applications, due to the need for high gain and small antenna footprint, far-field parameters like the aperture efficiency of the antenna, and the 1 dB gain bandwidth must be seen as important as the impedance matching (the -10 dB B.W.). The aperture efficiency can be seen as the appropriate figure of merit in evaluating a mm-wave antenna performance rather than the maximum gain. The aperture efficiency relates the maximum achieved gain to the area of the antenna in wavelengths (λ) [12] hence; high aperture efficiency indicates excellent utilization of an antenna footprint. This indeed fits well with the need for antennas of high gain; while occupying small areas for mm-wave applications. Another equally important parameter is the 1 dB gain bandwidth. This parameter unfortunately is not given enough consideration in many of the reported works in the open literature. It indicates the antenna's far-field performance's stability against frequency change, which is crucial at mm-wave frequencies. A narrow 1 dB gain bandwidth means a rapid change from the maximum gain achieved at close off-center frequencies. This also indicates considerable deformation occurs on the antenna far-field radiation pattern at off-center frequencies. Therefore, it is quite crucial at mm-wave frequencies to realize an excellent combination of the aforementioned figures of merit using a simple and compact antenna.

In this paper, we propose, analyze and validate a simple single-layer metamaterial lens with negative refractive index behaviour. This behaviour is shown to improve the focusing characteristics of the lens as compared to other lenses available in the open literature leading to owning the highest aperture efficiency; while maintaining a very competitive 1 dB gain B.W. as well as a 10 dB broad 10B impedance

bandwidth. Due to the low-loss nature of the proposed meta-lens, the radiation efficiency values sit above 90% at many frequencies with a maximum value of 95% at 28 GHz.

This paper is organized as follows: Section II presents the design considerations and analysis of the unit cell used to design the metamaterial lens. An analysis of the unit-cell negative refractive index behaviour and its equivalent circuit model is also discussed in Section II. Section III addresses the design of the entire 8 × 8 element meta-lens and illustrates how it is used to improve the performance of a single-slotted patch antenna. Section IV presents a discussion of simulated and measured results, antenna performance, and other antenna radiation characteristics. Section V summarizes the current state-of-the-art with respect to the proposed work. Finally, Section VI concludes the paper.

II. DESIGN AND ANALYSIS OF THE LENS UNIT-CELL

This section presents the geometry of the proposed meta-lens unit cell with a ring element. The transmission characteristics of an infinite periodic structure comprised of the proposed unit cell is analyzed, and accordingly, the selection of design parameters is justified. The negative refractive index behaviour of the meta-lens unit-cell is then discussed to reason its novel focusing ability that makes it optimum for gain enhancement at mm-wave frequencies.

A. THE PROPOSED LENS UNIT-CELL DESIGN CONSIDERATIONS AND TRANSMISSION CHARACTERISTICS

Despite the use of split ring resonators in antennas design is not new [4], [6], the use of a simple split ring resonator printed on a highly capacitive material arranged in a subwavelength lattice for millimeter wave applications, can be considered new, in particular, for mm-wave 5G applications. Fig. 1(a) shows the unit cell model of the proposed element as part of a periodic arrangement created using the ANSYS High-Frequency Structure Simulator (HFSS) [22]. The unit-cell is placed inside a waveguide with perfect magnetic conductors (PMC) assigned as a boundary condition to the *y*-*z* walls of the model. In contrast, perfect electric conductor boundaries (PEC) are applied to the walls in the *x*-*z* plane orthogonal to the incident electric fields. A linearly *y*-polarized TEM wave is then incident from wave port #1 on the top side, allowing for transmission and reflection coefficients prediction at both port#1 and port#2.

The reference planes of both ports are defined at the top surface of the ring element. The mm-wave lens unit cell is composed, as shown in Fig. 1(b), of a split ring of length L_{ring}, track width of W_{ring}, metallization thickness *t,* and gap width $\boldsymbol{g}$. The substrate used is Rogers TMM 10 (tm), which has a relative permittivity of 9.2, tangential losses of 0.0022, and a commercially available thickness of $d = 1.27$ mm. Unlike the design of mm-wave antennas of quite large aperture antennas, like transmitarrays and reflectarrays [23], [24], the use of such high capacitive material is economically feasible for small antennas; while the high relative permittivity

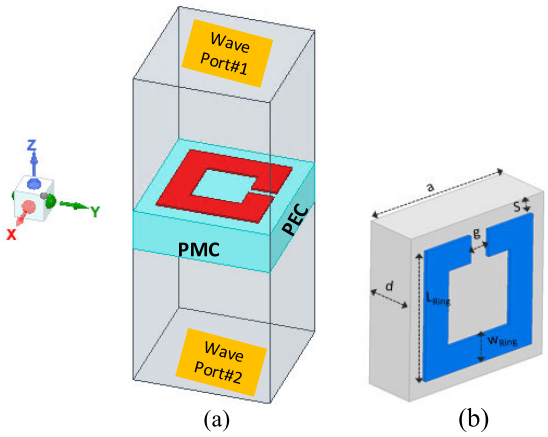

FIGURE 1. a) Full-wave HFSS model used for S-parameters extraction, b) Split ring resonator element design parameters.

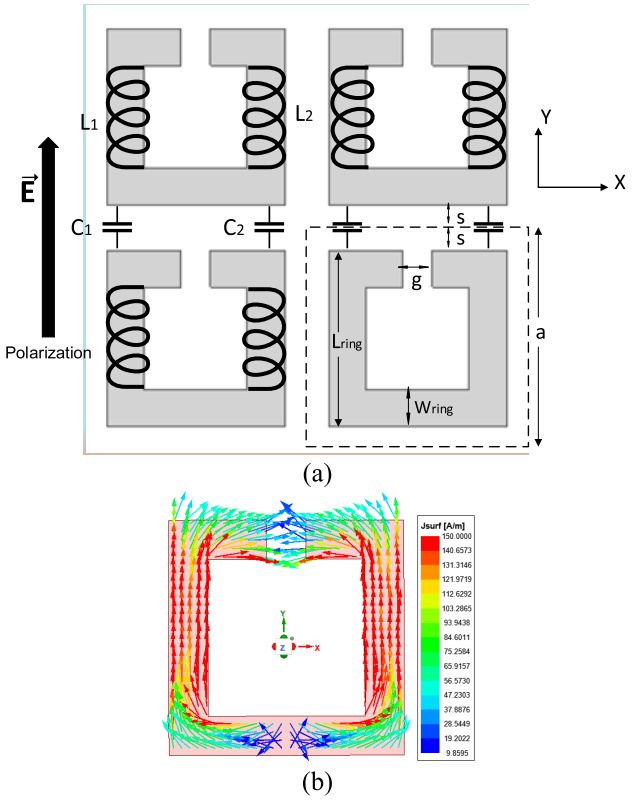

FIGURE 2. a) An equivalent circuit model of adjacent unit-cells of square split rings; b) Vector surface current density calculated at 28 GHz on the top surface of the proposed element with a=1.6 mm g=0.2 mm and W_{ring} = 0.25 mm and a copper thickness of t=35 μm.

is utilized to accommodate more radiating elements within a small footprint area. This can be seen as a way to achieve a sort of miniaturization as it reduces the unit-cell size a and hence the length of the ring length L_{ring}. This also fits well with the lens's targeted negative refractive index behavior as the use of a subwavelength (a small fraction of a free space wavelength) unit-cell can support the restoration of the amplitude of evanescent waves and therefore enable subwavelength

focusing [25]. The proposed equivalent circuit, shown in Fig. 2(a), helped much in understanding the proposed element operation and the selection of all design element parameters namely, W_{ring}, a, S and g except for the SRR length (L_{ring}). L_{ring} was selected to be a quarter effective wavelength (λ_{eff} /4) at 28GHz to support a strong resonance behavior, which is manifested by the current distribution shown in Fig. 2(b). The simple expressions that are used in calculating the effective wavelength, and consequently L_{ring} [26] are $\lambda_{eff} = (\lambda_o/\varepsilon_{eff})$, $L_{ring} = (\lambda_{eff}/4)$, respectively.

At a center frequency of 28 GHz, the calculated ε_{eff} and λ_{eff}, are 5.1 mm and 4.45 mm, respectively. The selected value of L_{ring} in this work is 1.2 mm. In [27] an equivalent circuit model was proposed and verified for an array of identical square ring elements (loops) printed on a grounded dielectric substrate based on models reported in [28]. Rationally, in [27] and [28], inductors were used to represent the metallic arms of the square ring element along the polarization direction, and gaps between adjacent elements were replaced by coupling capacitors.

For an array of very closely spaced split rings, we conjecture that the scenario is similar but with the gap introduced to tune the strong coupling between adjacent elements and to support the negative refractive index behaviour as explained in part B of this Section. A cursory look at the vector surface current distribution shown in Fig.2 (b), which is shown for one element as part of an infinitely periodic environment of identical elements, reveals explicitly that the vertical arms of the split ring resonator accommodate strong currents oriented along the direction of polarization. Not surprisingly, these time-varying currents will generate magnetic fields transverse to the current path and consequently to the incident electric field thus L_1 and L_2 are used to represent those arms in Fig. 2(a). On the other hand, the current distribution on the top and bottom arms of the ring, curls oppositely around the axis of symmetry (y-axis), thus the x-components of these currents cancel each other out; while the y-components survive and generate y-polarized electric near fields that are responsible for coupling between adjacent elements along the polarization direction. This explanation ties well with the polarity of charges indicated by current distribution; heads on the top arm and tails on the bottom arm. One can then introduce capacitors C_1 and C_2 between elements along the polarization direction to the left and right sides of the slit (the gap of width g). The slit will be shown useful in tuning the said coupling. The equivalent circuit model produced a periodic impedance surface comprised of an inductance $L = L_1 + L_2$ with total coupling capacitance $C = C_1 + C_2$. Luckily, while the length of the element L_{ring} is selected to yield resonance behavior, as pointed out earlier, expressions given in [27] and [28], for L and C reveal that W_{ring}, a, and S can be used to control the values of L and C, respectively, and hence control the impedance on the lens surface.

Since a and S control the spacing between elements, as revealed by Fig. 2(a), while L_{ring} is constant, the change in the unit cell size (a) would control C values. This occurs as

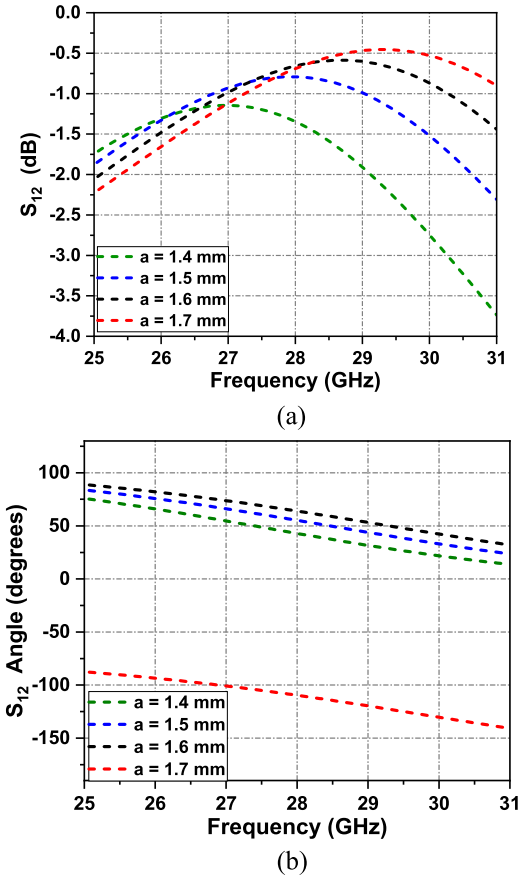

FIGURE 3. Effect of unit cell size a change on transmission coefficient (S_{12}). a) S_{12} magnitude versus frequency, b) S_{12} phase versus frequency.

TABLE 1. Design parameters used in unit-cell design.

Parameter Name	Parameter Symbol	Size (mm)
Ring Width	W_{ring}	0.4
Ring Length	L_{ring}	1.2
Slit Width	g	0.2
Substrate Height	d	1.27

the change in S is directly covered by the unit cell size change. On the other hand, adding a non-radiating slit with width g can add another degree of freedom to tune the capacitance value as it controls the width of capacitive edges. For constant L_{ring}, and selected a and g values, W_{ring} would be the main parameter to tune the element inductance. It is illustrated next how parameters a, and hence S, g, and W_{ring} are selected based on their effects on the transmission characteristics of the lens unit cell.

First, all designed parameters are fixed, except the unit-cell size a, as given in Table 1, and the effect of changing the unit-cell size is studied. Fig. 3(a) shows the predicted transmission coefficient magnitude at different unit-cell sizes. It is noticeable that the transmission magnitude improves with the increase in the unit-cell size. It exceeds -1 dB over a

wideband for $a = 1.6$ mm and $a = 1.7$ mm, respectively, and it even approaches -0.5 dB and beyond at some other frequencies. This means the transmission magnitude exceeds 0.9 to 0.95, this will lead to excellent power transmission through the meta-lens at a wide range of frequencies. A unit-cell size of $a = 1.6$ mm is selected for the lens design in this work as it exhibits better performance below 28 GHz while having a smaller subwavelength period. The transmission magnitude improvement against the increase in the unit-cell size stems from the fact that it reduces the coupling capacitance and produces more balance with the inductance generated along the loop.

A lens design also requires a slow change in the transmission coefficient phase versus frequency to avoid significant phase errors on a lens's surface. Phase errors lead to far-field deformations and hence poor gain values, associated with quite a narrow gain B.W., at off-center frequencies. The phase behavior versus frequency at several unit-cell sizes exhibited in Fig. 3(b), shows linear and stable variation with a phase change of around 8 degrees/GHz. This quite desirable behaviour will lead to stable far-field radiation hence, broadband gain operation.

Next, the effect of the slit width (g) and the ring width (W_{ring}) on the lens unit-cell transmittance is investigated. Fig. 4 shows progressive improvement in S_{12} magnitude as W_{ring} increases. For $W_{ring} = 0.4$ mm, the S_{12} magnitude is very promising, with values exceeding -1 dB from 27 to 30 GHz and sitting above -1.5 dB from 26 to 31 GHz. Smaller W_{ring} values, namely, $W_{ring} = 0.3$ mm and 0.2 mm are associated with higher inductance values that degrade S_{12} magnitude, especially beyond 27 GHz. On the other hand, the change in slit width (g) exhibits less effect on S_{12} magnitude as compared to W_{ring}. For $g = 0.2$ mm, the S_{12} magnitude is improved compared to $g = 0.1$ mm. This fine-tuning in S_{12} magnitude, which is concluded from the difference between solid and dashed lines in Fig. 4, looks more significant at smaller W_{ring} values as the slit width balances the larger inductance effect (at smaller W_{ring}). Therefore, $W_{ring} = 0.4$ mm and g = 0.2 mm were selected for the meta-lens unit-cell design as listed in Table 1.

The calculated transmitted, reflected, and absorbed (lost) powers for the meta-lens unit-cell are shown in Fig. 5. Expressions given in [29], which count for the power loss, were used to calculate the powers from the extracted S-parameters matrix of the lens full-wave model. The transmitted power shown in Fig. 5 (a), confirms the excellent transmittance of the lens within the targeted frequency band. It is evident that more than 80 % of the power passed through the lens in the band from 27-30 GHz whereas the maximum transmitted power exceeded 85 % between 28-29 GHz.

Considering that the lens is designed with negative refractive index behavior, even the 70% transmitted power between 26-27 GHz and 30-31 GHz would yield good operation due to the meta-lens excellent power focusing. The behavior of the transmitted power and reflected power against W_{ring} change, ties well with the S_{12} magnitude shown in Fig. 5. It is quite

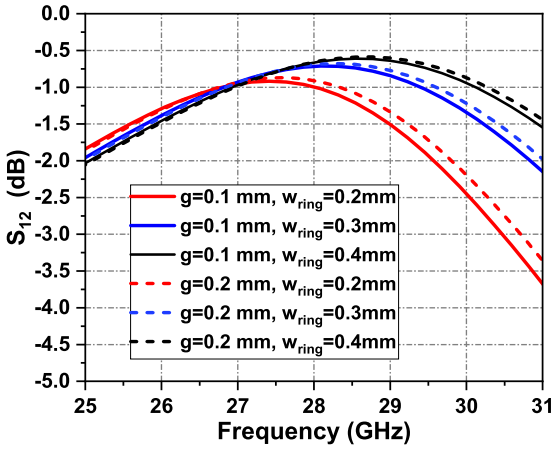

FIGURE 4. Effect of changing slit width (g) and ring width (w_{ring}) on transmission coefficient magnitude. S_{21}.

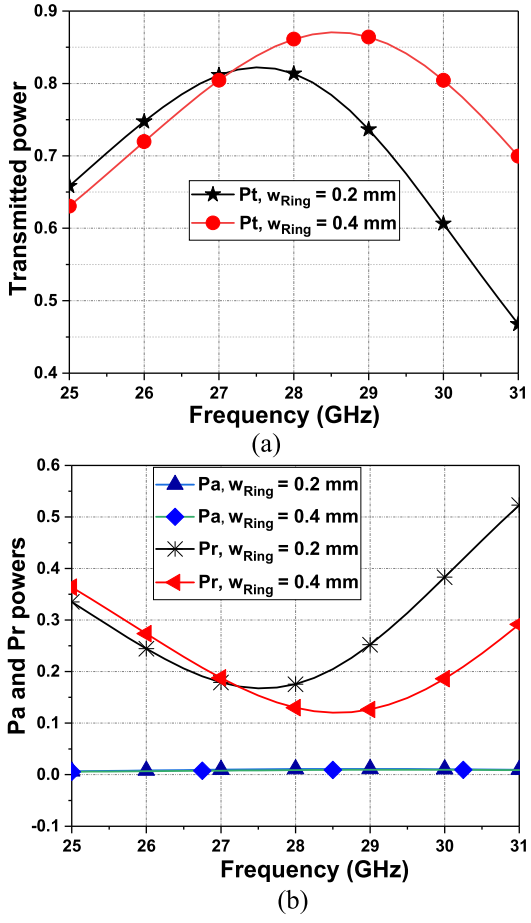

FIGURE 5. a) Transmitted power through meta-lens, b) reflected and absorbed powers.

clear that tuning in W_{ring} is crucial for successful lens design. Finally, the absorbed power (consumed power), shown in Fig.5 (b) confirms the very low loss nature of the proposed meta-lens despite the copper loss and tangent loss all included in the full-wave simulation model. The maximum power loss

resides in the range of 1-1.25% over the entire band. This indicates that the meta-lens will not degrade the radiation efficiency of the exciting antenna element as detailed in Section III.

B. THE META-LENS UNIT-CELL NEGATIVE REFRACTIVE INDEX BEHAVIOR

A negative index material is a material that generates negative effective permittivity and negative effective permeability concurrently over some frequency band [30]. A negative refractive index allows a flat lens to bring E.M. waves into focus, whereas conventional materials always require curved surfaces to focus E.M. waves [25]. Although such a material does not exist, its characteristics can be artificially emulated using a certain type of radiating elements when printed on some dielectric slabs, which was experimentally demonstrated in [31]. The attractive focusing ability of negative index material, and hence the potential of using it as a focusing lens, was reported in [25]. Regarding Fig. 6, it was established in [25] that the refraction angle (α) is always negative with respect to the surface normal hence, the E.M. wave diverging from the source, which has an incident angle (β), will be converged effectively beyond the lens interface leading to more wave collimation at close point(s) from the lens surface. Such a phenomenon will be illustrated in Section III using the predicted total electric near-field near the lens surface. Despite the work done in [25] deals with optical frequencies, optical principles were shown valid, despite being approximate, for antennas' design at mm-wave frequencies [32], [33].

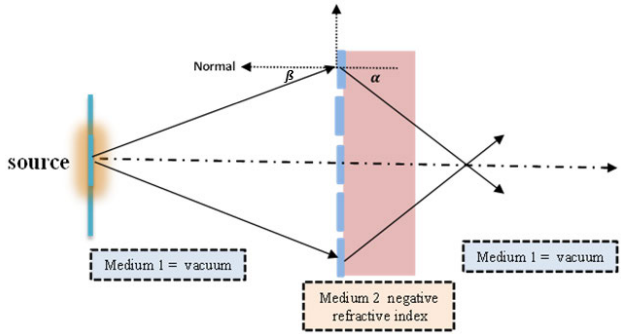

FIGURE 6. Proposed lens operation based on negative refractive index effect. [adapted after 26].

The calculated refractive index and effective constitutive parameters for the proposed meta-lens unit cell shown in Fig. 1, using the design parameters given in Table 1, are depicted in Fig. 7. Equations (1), (2) and (3) [34] given below were used to calculate the effective permittivity (ε_{eff}), effective permeability (μ_{eff}) and the effective refractive index (n_{eff}) from the extracted S-parameters matrix at many frequencies from 25 GHz to 31 GHz.

$$n_{eff} = \frac{1}{kd}\cos^{-1}\left[\frac{1}{2S_{21}}\left(1 - S_{11}^2 + S_{21}^2\right)\right] \quad (1)$$

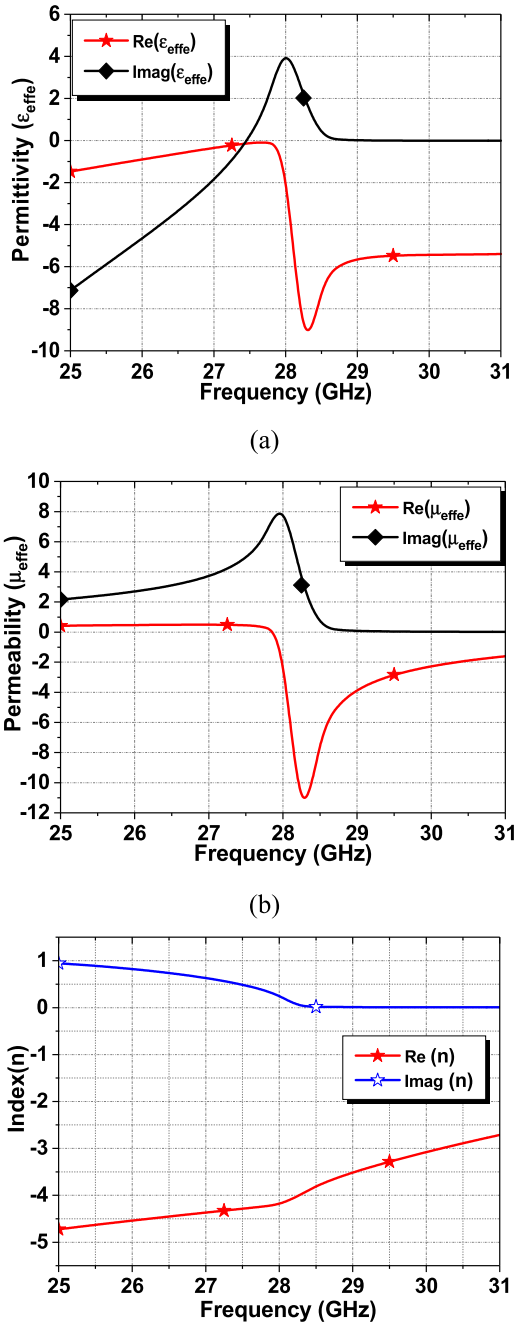

FIGURE 7. Calculated constitutive effective parameters of the meta-lens unit cell. a) Effective permittivity, b) effective permeability, and c) effective refractive index. All are calculated from extracted scattering parameters for unit cell design parameters given in Table 1.

$$Z = \sqrt{\frac{(1+S_{11})^2 - S_{21}^2}{(1-S_{11})^2 - S_{21}^2}}, \quad (2)$$

$$\varepsilon_{eff} = \frac{n_{eff}}{z}, \quad \mu_{eff} = n_{eff} Z \quad (3)$$

where k and d are the propagation constant and the thickness of the metamaterial lens, respectively. Fig. 7(c) shows that the structure has a negative index region that extends over

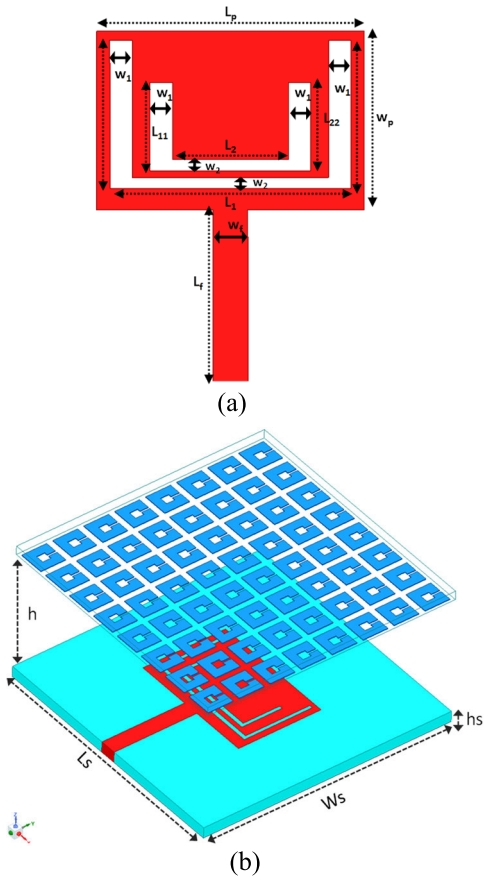

FIGURE 8. The proposed antenna model a) slotted patch, b) slotted patch, and the meta-lens. Parameters' dimensions are: Lp = 6, Wp = 4, t = 0.035, L_{11} = 3.11, W_1 = 0.17, W_2 = 0.175, L_1 = 5.06, L_2 = 4.1, L_{22} = 1.76, hs = 0.508, Ws = Ls = 12.8. (units = mm).

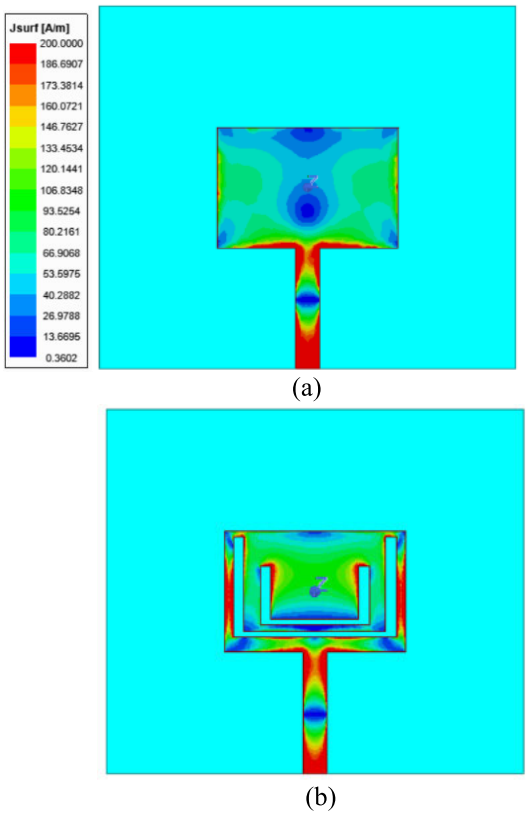

FIGURE 9. The Surface current distribution was calculated at 28 GHz on a, a) simple patch and b) slotted patch.

the whole frequency band from 25 to 31 GHz. Therefore, the meta-lens own negative refractive behavior, as confirmed by the results in Fig. 7. This would, as pointed out earlier, entail negative refractive angles that allow for more convergence and focusing of the incident waves; hence, the resulting refraction angle α must be negative with respect to the surface normal. Consequently, this will improve the incident wave focusing leading to real antenna gain and aperture efficiency enhancement. Fig. 7(a) and Fig. 7(b) exhibit drastic change in ε_{eff} and μ_{eff} near resonance (28 GHz), and more interestingly, the real ε_{eff} and μ_{eff} have close values from 27 to 29 GHz. This may indicate good matching

to free space impedance and hence better transmission characteristics within the said frequency band. Since only one split ring element is used in the proposed lens, while the incident electric field is polarized along the slit, one can observe the meta-lens produces a full negative electric response as shown in Fig. 7(a).

III. WIDE-BAND HIGH-GAIN META-LENS ANTENNA CONFIGURATION AND CHARACTERIZATION

A. ANTENNA CONFIGURATION

To use the proposed meta-lens as a superstrate for gain and hence aperture efficiency enhancement, the unit-cells are arranged in an array with a periodicity of 8 × 8 to form a single layer of negative refractive index material. The lens is placed in the near-field region closely above a slotted microstrip patch antenna at a distance of h as shown in the antenna perspective view in Fig. 8(b). This study uses a slotted patch reported in [36] to excite the meta-lens. As shown in Fig. 8(a), the slotted patch has two U-shaped slots engraved on a rectangular patch that is fed by a microstrip line and printed on a Rogers RT/Duroid 5880 substrate with a dielectric constant $\varepsilon_r = 2.2$ and a thickness $hs = 0.508$ mm. All slotted patch parameters dimensions are given in the Fig. 8 caption.

The spacing, from the radiator (slotted patch) to the bottom side of the metamaterial superstrate is h. This is optimized to obtain better antenna performance as detailed in part B of this section. The metamaterial superstrate layer is of a standard thickness $d = 1.27$ mm. The antenna ground plane and metamaterial superstrate have dimensions of $12.8 \times 12.8 \times 7.27\text{mm}^3$ ($1.2\ \lambda \times 1.2\ \lambda \times 0.68\ \lambda$, where λ is the free space wavelength at 28 GHz). These dimensions are changed a bit upon fabrication hence, calculated aperture efficiency was made based on a footprint of $1.25\ \lambda \times 1.3\ \lambda$.

The slotted patch is used in this work to improve the poor matching obtained from a simple patch designed at 28 GHz. The slots improve the impedance matching by altering the current distribution on the patch. The extracted surface currents on the simple patch and the slotted patch calculated

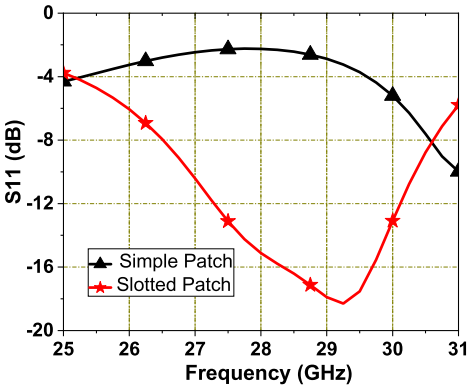

(a)

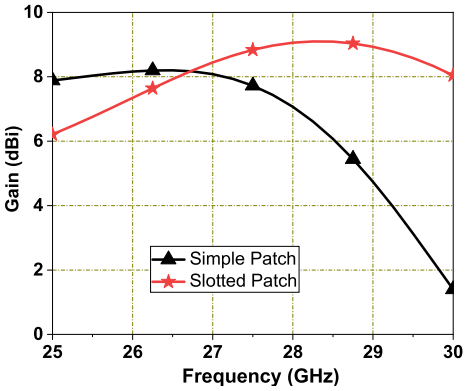

(b)

FIGURE 10. a) Calculated S11 versus the frequency of the simple patch and the slotted patch. b) Calculated gain versus frequency of the simple patch and the slotted patch.

at 28 GHz are shown in Fig. 9(a) and Fig. 9(b), respectively. It is evident that adding slots to the patch changed the current distribution and hence improved the resonant effect by increasing the current densities at the radiating edges of the slotted patch as compared to the simple patch.

Upon the optimization of the U slots' location and dimension, the S_{11} was significantly improved over the entire band and the radiation from the two U slots improved the patch antenna gain as shown in Fig.10 (a) and Fig. 10(b), respectively.

The selection of the 8×8 array size for the proposed meta-lens was at first mainly governed by the antenna aperture size, which equals 13mm, and the optimized unit cell size, which equals 1.6mm selected based on the results shown in Fig. 3; these figures entails an array size of 8×8 ($13/1.6 = 8$). However, it is tentatively known in advance that a smaller array size than 8×8 may result in a smaller gain due to the less focusing of the radiation emanating from the slotted patch antenna while a larger array will be oversized with respect to the slotted patch antenna and hence may reduce the antenna aperture efficiency. To investigate the effect of the array size on the meta-lens performance, 6×6 and 10×10 array meta-lenses were designed and simulated. Fig. 11(a) and Fig. 11(b) show the 3D models of the 6×6 meta-lens

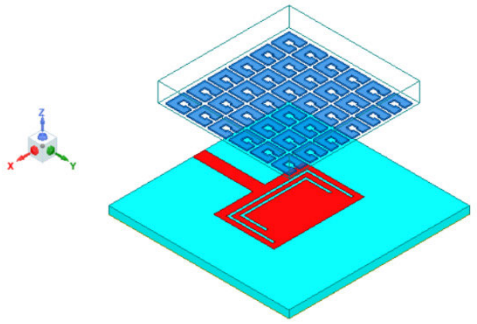

(a)

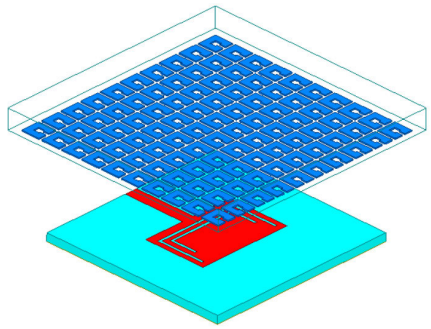

(b)

FIGURE 11. 3D HFSS model for a) 6×6 array meta-lens and b) 10×10 array meta-lens.

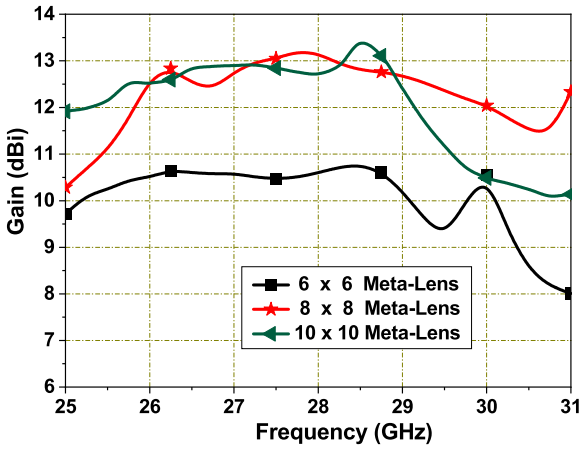

FIGURE 12. The calculated gain versus frequencies of the meta-lens at different array sizes.

and the 10×10 meta-lens, respectively. Fig. 12 exhibits the calculated gain versus frequency when the meta-lens of the concerned sizes are placed on top of the slotted patch antenna. It is clear that the 8×8 array substantially outperforms the 6×6 array meta-lens while it provides overly close to better performance as compared to the 10×10 array meta-lens. This makes the 8×8 array size a viable choice for the proposed SRR meta-lens.

B. COMPLETE ANTENNA CHARACTERIZATION AND PERFORMANCE ANALYSIS

Next, the effect of changing the spacing h between the slotted patch and the meta-lens is investigated. Fig. 13(a) exhibits

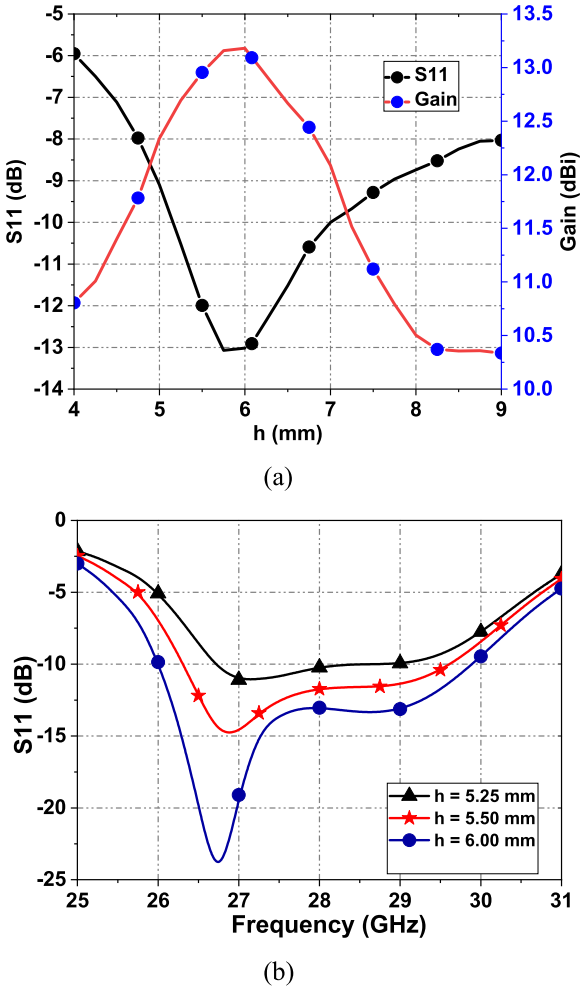

FIGURE 13. a) Effect of changing the vertical spacing (*h*) between the slotted patch and meta-lens on the gain and reflection coefficient at 28 GHz., b) Effect of changing *h* on the impedance matching over the entire band.

the change of the antenna gain and reflection coefficient (S_{11}) versus *h*. It is evident that *h* values slightly below 6 mm provide the best gain-S_{11} combination; hence $h = 5.9$ mm was selected for antenna simulation and measurement. Apparently, within the close vicinity of $h = 5.9$ mm the transmission through the lens is excellent as the gain is high and the reflection is reasonably low. The strong effect of changing *h* on the impedance matching over the entire band is illustrated in Fig. 13(b).

Fig. 14(a) shows the fabricated prototype and Fig. 14(b) shows the slotted patch mounted for measurement in a far-field anechoic chamber. The measurement was done using a standard far-field chamber in which the received power at the Antenna under Test (AUT) emanated from a Ka-band horn antenna is used to predict the principle pattern cuts. The AUT gain was measured using the gain substitution method by comparing the received power by the AUT to the received power by a reference antenna of known gain.

Fig. 15 shows the antenna's measured versus calculated S_{11} values over the entire band. Both curves in Fig. 15 compare

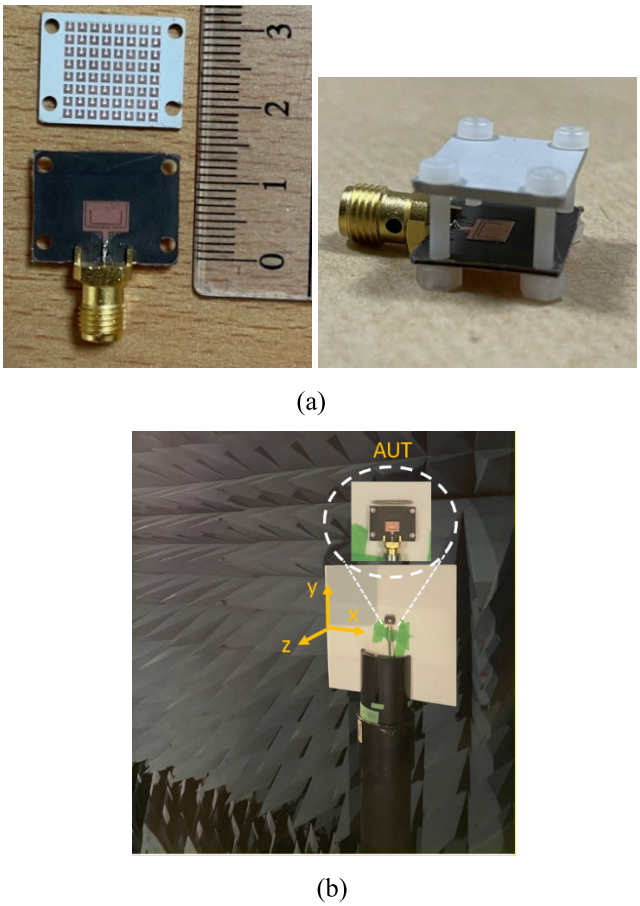

FIGURE 14. a) Fabricated antenna prototype before and after assembly and b) slotted patch antenna mounted for measurement.

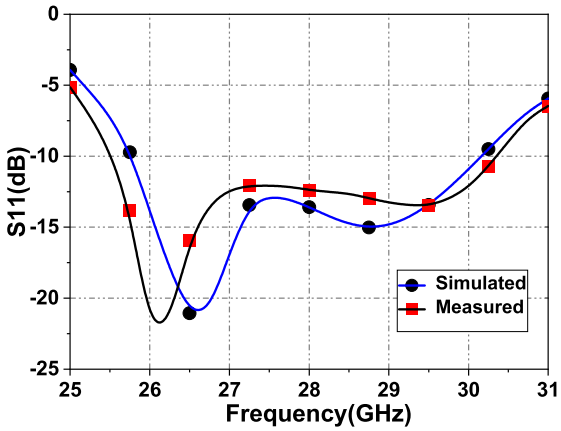

FIGURE 15. Measured versus simulated S11 (dB).

well and follow the same changing trend, except the shift toward lower frequencies resulted from measurement. Upon a microscopic check of the etching tolerance of the split rings, there was a systematic error that might have created such a frequency shift. The -10dB fractional B.W. predicted from the measured results equals 17%. This is quite reasonable as compared to the ones obtained in works for mm-wave applications.

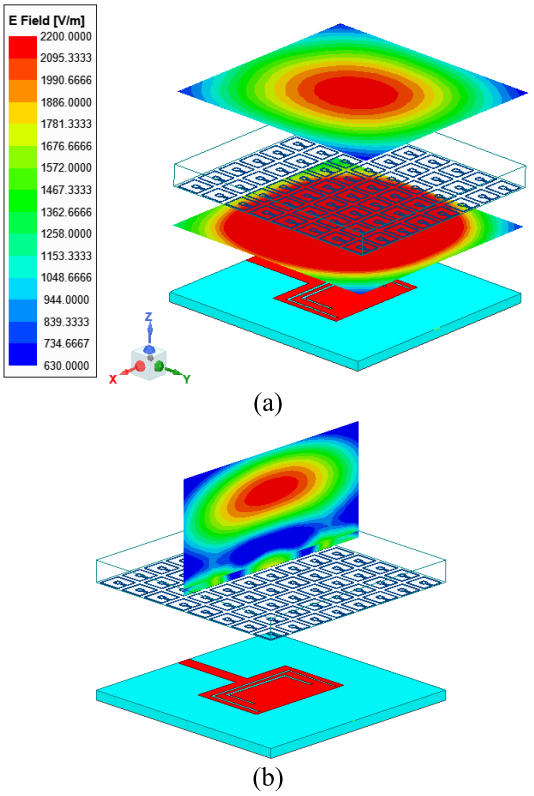

FIGURE 16. Proposed meta-lens focusing on the incident fields from the slotted patch. The magnitude of total near fields are predicted at 28 GHz on a) parallel 2D cuts to the lens surface and b) an orthogonal plane to the lens surface at the transmission side.

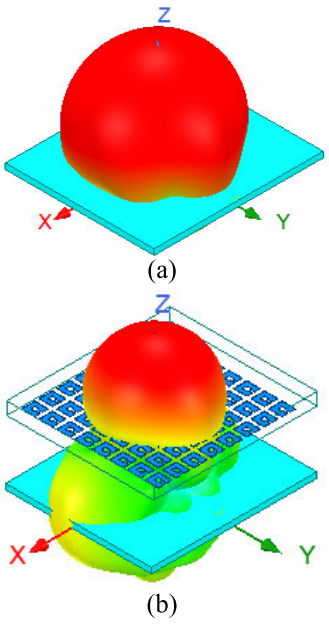

FIGURE 17. 3D Far-field radiation pattern a) slotted patch alone b) meta-lens on top of the slotted patch.

To illustrate the excellent focusing characteristics of the meta-lens, the total near-fields were predicted on different planes close to the lens surface. In Fig. 16(a), the

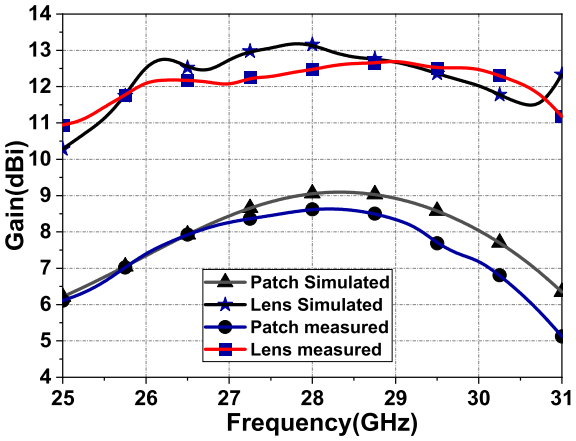

FIGURE 18. Measured versus simulated gain values (dBi) versus frequency for both the slotted patch alone and the entire antenna.

near-fields predicted on planes parallel to the lens surface, one below and the other above the lens, show explicitly how the wildly scattered electric fields emanated from the slotted patch were focused efficiently to converge over a much smaller zone on the transmission side of the lens, which looks like a focal region. The formation of the said focal region, and hence the strong focusing effect of the meta-lens, becomes very obvious from the fields depicted in Fig. 16(b) where the field is predicted on an orthogonal plane, which cuts through the plane in Fig.16(a), in the transmission side of the lens. These observations strongly support the argument that the negative refractive index leads to negative refractive angles as discussed in Section II-B and reported in [25]. A focal point was indeed obtained at mm-wave frequencies, which confirms the strong focusing effect caused by the negative refractive index behaviour of the meta-lens.

The 3D far-filed radiation patterns shown in Fig. 17 tie well with the near-fields in Fig. 16. It is quite clear how the use of the meta-lens narrowed the broad far-field pattern of the slotted patch alone to a much more directive beam. The gain behaviour versus frequency is shown in Fig. 18. The measured gain values compare well to the simulated ones for both the patch alone and the entire antenna comprised of the meta-lens on top of the patch. The maximum measured gain is 12.7 dBi, while the aperture efficiency at this gain is 92%. These excellent metrics slightly change at off-center frequencies, as the measured 1dB gain bandwidth is 18%. Finally, Fig. 19 exhibits the measured versus simulated normalized far-field principle planes pattern cuts at frequencies 26 GHz, 27 GHz, and 28 GHz, respectively. The measured patterns have good agreement with simulated ones with some discrepancies that can be attributed to some slight misalignment of the antenna during measurement and to the gain reduction at some measured frequencies as compared to the simulated ones. Overall, it is evident that the antenna performance is stable versus frequency.

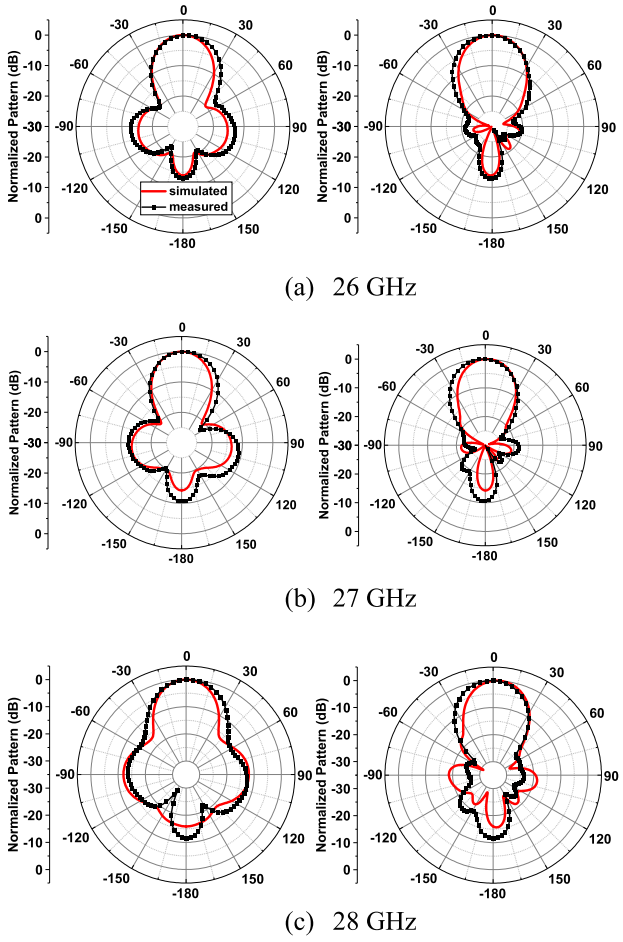

FIGURE 19. Measured versus calculated E-plane cuts (left) and H- plane cuts (right) at different frequencies.

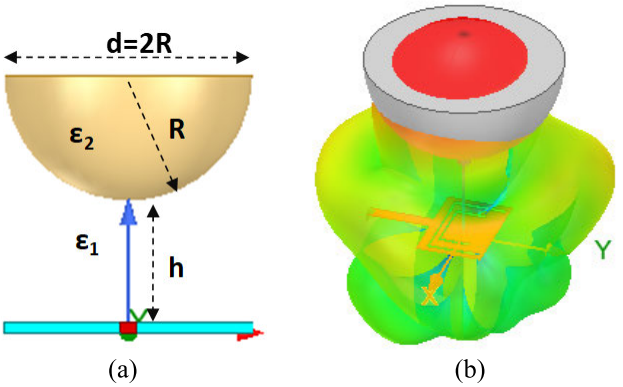

FIGURE 20. An equivalent conventional lens to the proposed SRR meta-lens, a) conventional lens design parameters b) calculated 3D radiation pattern using the conventional lens at 28GHz.

C. THE META-LENS PERFORMANCE VERSUS A CONVENTIONAL LENS

The performance of the meta-lens is then compared to an equivalent conventional lens of the same footprint. A spherical conventional lens was designed [37] using equation (4) [37]. The dielectric material used is polytetrafluoroethylene (PTFE) with $\varepsilon_2 = 2.2$, which is common for lens design.

$$h \cong \left(\frac{\sqrt{\varepsilon_1}}{\sqrt{\varepsilon_2} - \sqrt{\varepsilon_1}} - 1\right) R \tag{4}$$

In (4), ε_1 and ε_2 are the relative dielectric permittivity of the free space and the lens material, respectively, and h = 5.9mm. The slotted patch antenna, as shown in Fig. 20, is used to excite the conventional lens and the structure is fully simulated using HFSS [22].

The simulated results of the gain and S_{11} are compared in Fig. 21 for the conventional lens versus the proposed SRR meta-lens, respectively. It is clear that the meta-lens and the conventional lens generate comparable gain values over the entire band with a slight gain improvement achieved by the meta-lens at some frequencies. Such higher gain values obtained by a flat lens as compared to an equivalent conventional lens are reported in [38]. Regarding the impedance matching, despite the conventional lens offering better matching from 27GHz to 30GHz (lower S_{11} values), the 10-dB fractional bandwidth of the SRR meta-lens is wider. These results confirm the good performance of the proposed meta-lens as it offers comparable performance to a conventional lens while it has a much smaller profile.

To further confirm the proposed meta-len's excellent focusing ability, a different source antenna was used to excite the meta-lens. The element was proposed in [9] to operate at mm-wave frequencies. Fig. 22 shows the antenna element with the proposed meta-lens located at h = 5.9mm on top of it. Fig. 23 exhibits the calculated gain values over the entire frequency band for the antennas alone and the antennas topped with the proposed meta-lens. Fig. 23 shows clearly that the SRR meta-lens functions very well in improving the gain for both types of antennas used to excite it. This is evident from the 4-5 dBi gain increase achieved over the entire band. This indeed further confirms the excellent focusing performance of the proposed SRR meta-lens irrespective of the considered antenna type used to excite it.

D. PROPOSED META-LENS POSSIBLE APPLICATION

As pointed out in the introduction, despite the millimeter wave (mm-wave) bands in the range of 25-40 GHz being licensed for a decade, the existing technology (4G/WiFi/WLAN) is still using microwave sub-6GHz bands due to the challenges associated with mm-wave network implementation and the strong signal fading at mm-wave frequencies. Despite this, we strongly believe that mm-wave wireless communication systems will be implemented worldwide within the coming years due to the aggressive demand for higher data rates.

Regarding the possible applications of the proposed meta-lens antenna, the focus of the scientific literature thus far has been on designing mm-wave antennas for base station platforms [39] and mobile phones [40]. However, authors strongly believe that mm-wave implementations will not be

TABLE 2. Performances comparison between the proposed antenna and the current state-of-the-art.

Ref.	Lens/ Metasurface Structure	Antenna Element	Frequency Band (Center) GHz	10 dB B.W.%B. W.(%)	Footprint (area) (W × L)	Max Gain dBi	1dB Gain BW	Aperture Efficiency %	Radiation Efficiency %
[9]	Single Layer of square rings	Patch antenna	24.2 – 29.5 (27.5)	34.7	1.1λ × 1.1λ	11	NA	83	NA
[4]	Three layers of split rings	Magneto-electric (ME) dipole	20 – 40 (29.5)	22.5	1.18 λ × 0.88 λ	10.5	13%	86	93
[10]	Single layer of circular split rings	Square dense dielectric patch	26 – 30.5 (30)	15.3	2.9 λ × 2.9 λ	15.4	4 %	33	90
[16]	Single layer of curved strips	Yagi antenna with EBG	25 – 33 (29.5)	17.2	13.7 λ ×13.7 λ	11.9	NA	20	94
[11]	Single layer of patches	Slot-Metasurface with SIW feeding	24.3 – 27.5 (26.5) / 37 – 40.5 (38.9)	20.7/ 11.3	2.8 λ ×1.5 λ	7.4 /10.9	NA	24/	90
[5]	Single layer EBG surface	Slotted patch with EBG	20 – 40 (28)	40	2.6 λ × 3.1 λ	15	NA	32	N.A.
[*]	**Single Layer of split rings**	**Slotted Patch**	**25-31 (28 GHz)**	**17**	**1.25λ ×1.3λ**	**12.7**	**18%**	**92**	**95**

restricted to cell phone networks, and will be extended to replace the current indoor WiFi 4G and Sub-6GHz systems. This is natural as there is no point in implementing a very expensive mm-wave 5G network without upgrading all terminal devices despite both 4G and 5G systems can stay functional simultaneously. This will certainly require access points and routers with antennas of much higher gain values than the existing ones used in the 4G and Sub 6G spectrums, which are typically in the 4-6 dBi range [41], to provide an acceptable power level at the terminals of the receiving device (like cell phones, tablets, and laptops). Therefore, the proposed antenna can be used for routers and access points at mm-wave frequencies as the achieved gain range (11-12.7 dBi) is quite reasonable to overcome fast fading in indoor environments like big halls and meeting rooms. To ensure full coverage and polarization diversity multiple of the proposed antennas can fit easily on the side, top, or bottom facets of an access point with different orientations [41]. An illustration of such an implementation can be grasped from Fig. 24 shown below. Radiation patterns can be titled mechanically as illustrated by shaping the access point chassis or by defining phase gradients on the meta-lens surface similar to the principle explained in [42].

IV. STATE OF-THE-ART COMPARISON

In order to highlight the merits of the proposed design compared to previous related works, Table 2 compares the performances of some recent millimeter-wave antennas that utilize a lens or a metasurface to improve the gain and/or the bandwidth of another antenna element. It is evident from Table 2 that the aperture efficiency of the proposed design (92%) is the highest among all works. This indeed came as a result of the excellent focusing characteristic generated by the selected meta-lens. To our knowledge, this is the highest aperture efficiency value available in the open literature for similar antennas. It is worth mentioning here that the aperture efficiency was calculated, for all antennas in Table 2, using the expression given for aperture efficiency in [12] and based on the antenna area and maximum measured gain values reported in the corresponding references.

One can also realize that the proposed antenna provides the best impedance-bandwidth/gain-bandwidth combination (17%/18%) despite other designs like the ones in [4] and [9] do provide higher 10dB B.W. alone. This good performance at the port level as well as in the farfield confirms, as reinforced by the far-field pattern stability illustrated in Section III, the superior performance of the proposed design. It is also obvious from the comparison table that the proposed design belongs to the group of antennas that have a quite small footprint [4], [9]. Moreover, the low loss nature of the negative refractive index material yielded a quite high radiation efficiency of a maximum value of 95%. This is the highest value among all recent designs reviewed in this paper. Finally, unlike many of the complex designs available in the

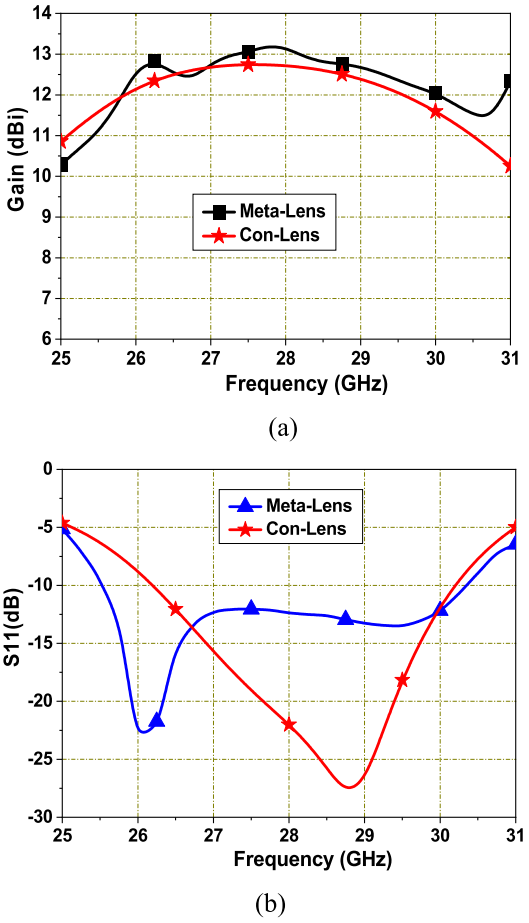

FIGURE 21. a) Calculated gain versus frequency of the proposed meta-lens against the equivalent conventional lens, b) calculated S11 versus frequency of the proposed meta-lens against the equivalent conventional lens.

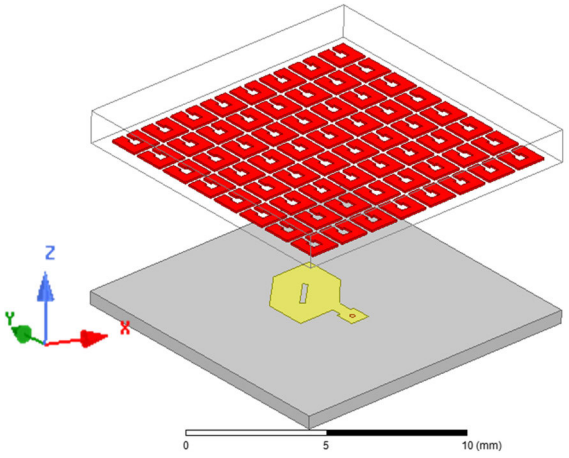

FIGURE 22. 3D HFSS Model of the proposed meta-lens used with the antenna proposed in [9].

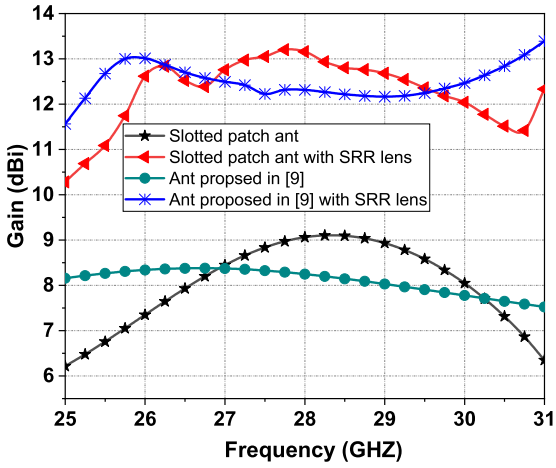

FIGURE 23. Gain improvement obtained using the proposed meta-lens for the slotted patch against the antenna proposed in [9].

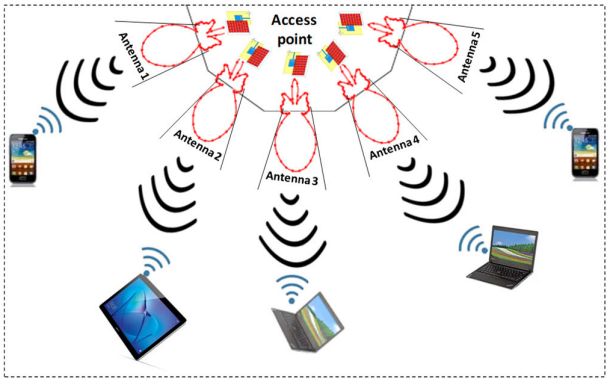

FIGURE 24. Possible implementation of the proposed meta-lens antenna in a future mm-wave access point.

open literature, the proposed design utilizes a simple single-layer meta-lens to improve the gain and bandwidth mounted on top of another simple slotted patch antenna. As listed in Table 2, most designs include some complexity either in the lens geometry or in the antenna element itself, except the proposed method and the design in [9].

V. CONCLUSION

A simple single-layer mm-wave meta-lens is proposed for 5G antenna performance enhancement. The proposed meta-lens is composed of 8 × 8 split ring elements that all occupy a minimal footprint of $1.25\lambda \times 1.3\lambda$. Hence, it can be considered one of the most compact lenses available in the open literature. Despite this small footprint, the proposed meta-lens were shown, via both simulation and measurement, to be very effective in improving the gain of a slotted patch antenna by 4-5 dBi over a wide frequency band from 25 GHz to 31 GHz. This was justified by the negative refractive index behavior that significantly improved the lens focusing characteristics. The achieved aperture efficiency of the proposed antenna, which is 92%, is the maximum reported in the literature for similar mm-wave antennas. This is a very desirable feature as it yields a high-gain antenna with quite a small footprint. The stability of the proposed antenna performance against frequency was established by producing a wide impedance bandwidth of 17% associated with a wide 1dB gain bandwidth of 18%. Such a combination is indeed novel, especially

because a high radiation efficiency accompanied it at many frequencies with a maximum value of 95%. Due to the simplicity, compactness, and excellent performance metrics, the proposed meta-lens represents a promising candidate for low-profile mm-wave 5G applications.

VI. ACKNOWLEDGMENT

The authors appreciate and acknowledge the support provided by the University of Sharjah, United Arab Emirates, by providing all their resources to conduct this research.

REFERENCES

[1] Federal Communications Commission (FCC). *The FCC's 5G FAST Plan, Spectrum*. Accessed: Oct. 2022. [Online]. Available: https://www.fcc.gov/5G

[2] T. S. Rappaport, S. Sun, R. Mayzus, H. Zhao, Y. Azar, K. Wang, G. N. Wong, J. K. Schulz, M. Samimi, and F. Gutierrez, "Millimeter wave mobile communications for 5G cellular: It will work!" *IEEE Access*, vol. 1, pp. 335–349, 2013.

[3] M. Ikram, K. Sultan, M. F. Lateef, and A. S. M. Alqadami, "A road towards 6G communication—A review of 5G antennas, arrays, and wearable devices," *Electronics*, vol. 11, no. 1, p. 169, 2022.

[4] A. Dadgarpour, M. Sharifi Sorkherizi, and A. A. Kishk, "High-efficient circularly polarized magnetoelectric dipole antenna for 5G applications using dual-polarized split-ring resonator lens," *IEEE Trans. Antennas Propag.*, vol. 65, no. 8, pp. 4263–4267, Aug. 2017.

[5] X. Lin, B.-C. Seet, F. Joseph, and E. Li, "Flexible fractal electromagnetic bandgap for millimeter-wave wearable antennas," *IEEE Antennas Wireless Propag. Lett.*, vol. 17, no. 7, pp. 1281–1285, Jul. 2018.

[6] F.-Y. Meng, Y.-L. Li, K. Zhang, Q. Wu, and J. L.-W. Li, "A detached zero index metamaterial lens for antenna gain enhancement," *Prog. Electromagn. Res.*, vol. 132, pp. 463–478, 2012.

[7] H. Zhou, Z. Pei, S. Qu, S. Zhang, J. Wang, Z. Duan, H. Ma, and Z. Xu, "A novel high-directivity microstrip patch antenna based on zero-index metamaterial," *IEEE Antennas Wireless Propag. Lett.*, vol. 8, pp. 538–541, 2009.

[8] G. Augustin, B. P. Chacko, and T. A. Denidni, "A zero-index metamaterial unit-cell for antenna gain enhancement," in *Proc. IEEE Antennas Propag. Soc. Int. Symp. (APSURSI)*, Jul. 2013, pp. 126–127.

[9] N. Hussain, M. Jeong, A. Abbas, T. Kim, and N. Kim, "A metasurface-based low-profile wideband circularly polarized patch antenna for 5G millimeter-wave systems," *IEEE Access*, vol. 8, pp. 22127–22135, 2020.

[10] M. Asaadi, I. Afifi, and A.-R. Sebak, "High gain and wideband high dense dielectric patch antenna using FSS superstrate for millimeter-wave applications," *IEEE Access*, vol. 6, pp. 38243–38250, 2018.

[11] T. Li and Z. N. Chen, "A dual-band metasurface antenna using characteristic mode analysis," *IEEE Trans. Antennas Propag.*, vol. 66, no. 10, pp. 5620–5624, Oct. 2018.

[12] A. K. Singh, M. P. Abegaonkar, and S. K. Koul, "High-gain and high-aperture-efficiency cavity resonator antenna using metamaterial superstrate," *IEEE Antennas Wireless Propag. Lett.*, vol. 16, pp. 2388–2391, 2017.

[13] B. Majumder, K. Kandasamy, and K. P. Ray, "A zero index based meta-lens loaded wideband directive antenna combined with reactive impedance surface," *IEEE Access*, vol. 6, pp. 28746–28754, 2018.

[14] K. Agarwal, N. Nasimuddin, and A. Alphones, "Wideband circularly polarized AMC reflector backed aperture antenna," *IEEE Trans. Antennas Propag.*, vol. 61, no. 3, pp. 1456–1461, Mar. 2013.

[15] M. Asif, D. A. Sehrai, S. H. Kiani, J. Khan, M. Abdullah, M. Ibrar, M. Alibakhshikenari, F. Falcone, and E. Limiti, "Design of a dual band SNG metamaterial based antenna for LTE 46/WLAN and Ka-band applications," *IEEE Access*, vol. 9, pp. 71553–71562, 2021.

[16] M. Mantash and T. A. Denidni, "CP antenna array with switching-beam capability using electromagnetic periodic structures for 5G applications," *IEEE Access*, vol. 7, pp. 26192–26199, 2019.

[17] W. A. Awan, S. I. Naqvi, A. H. Naqvi, S. M. Abbas, A. Zaidi, and N. Hussain, "Design and characterization of wideband printed antenna based on DGS for 28 GHz 5G applications," *J. Electromagn. Eng. Sci.*, vol. 21, no. 3, pp. 177–183, Jul. 2021.

[18] Y. Ge, K. P. Esselle, and T. S. Bird, "The use of simple thin partially reflective surfaces with positive reflection phase gradients to design wideband, low-profile EBG resonator antennas," *IEEE Trans. Antennas Propag.*, vol. 60, no. 2, pp. 743–750, Feb. 2012.

[19] M. Hussain, S. M. Rizvi, A. Abbas, A. Nadeem, I. Alam, and A. Iftikhar, "A wideband antenna for V-band applications in 5G communications," in *Proc. Int. Bhurban Conf. Appl. Sci. Technol. (IBCAST)*, Jan. 2021, pp. 1017–1019.

[20] N. Supreeyatitikul, T. Lertwiriyaprapa, and C. Phongcharoenpanich, "S-shaped metasurface-based wideband circularly polarized patch antenna for C-band applications," *IEEE Access*, vol. 9, pp. 23944–23955, 2021.

[21] W. Zhang, C. Song, R. Pei, Y. Huang, and J. Zhou, "Broadband metasurface antenna using hexagonal loop-shaped unit cells," *IEEE Access*, vol. 8, pp. 223797–223805, 2020.

[22] *Ansys HFSS*. Accessed: Oct. 2022. [Online]. Available: https://www.ansys.com

[23] G. Gosal, E. Almajali, D. McNamara, and M. Yagoub, "Transmitarray antenna design using forward and inverse neural network modeling," *IEEE Antennas Wireless Propag. Lett.*, vol. 15, pp. 1483–1486, 2016.

[24] E. Almajali, D. A. McNamara, J. Shaker, and R. Chaharmir, "Feed image lobes in offset-fed reflectarrays: Diagnosis and solution," *IEEE Trans. Antennas Propag.*, vol. 60, no. 1, pp. 216–227, Jan. 2015.

[25] J. B. Pendry, "Negative refraction makes a perfect lens," *Phys. Rev. Lett.*, vol. 85, no. 18, pp. 3966–3969, Oct. 2000.

[26] M. D. Pozar, *Microwave Engineering*, 4th ed. Hoboken, NJ, USA: Wiley, 2012.

[27] J. Ethier, M. R. Chaharmir, and J. Shaker, "Reflectarray design comprised of sub-wavelength coupled-resonant square loop elements," *Electron. Lett.*, vol. 47, no. 22, p. 1215, 2011.

[28] N. Marcuvitz, *Waveguide Handbook*. New York, NY, USA: McGraw-Hill, 1951.

[29] U. C. Hasar, J. J. Barroso, Y. Kaya, T. Karacali, and M. Ertugrul, "Investigation of transmitted, reflected, and absorbed powers of periodic and aperiodic multilayered structures composed of bi-anisotropic metamaterial slab and conventional material," *Photon. Nanostruct. Fundamentals Appl.*, vol. 13, pp. 106–119, Jan. 2015.

[30] D. R. Smith, W. J. Padilla, D. C. Vier, S. C. Nemat-Nasser, and S. Schultz, "Composite medium with simultaneously negative permeability and permittivity," *Phys. Rev. Lett.*, vol. 84, pp. 4184–4187, May 2000.

[31] R. A. Shelby, D. R. Smith, and S. Schultz, "Experimental verification of a negative index of refraction," *Science*, vol. 292, no. 5514, pp. 77–79, Apr. 2001.

[32] P. Checcachi, V. Russo, and A. Scheggi, "Holographic antennas," *IEEE Trans. Antennas Propag.*, vol. AP-18, no. 6, pp. 811–813, Nov. 1970.

[33] E. Almajali, D. McNamara, S. Alja'afreh, M. S. Sharawi, and I. Mabrouk, "A low-profile holographic antenna with dual-metasurface and printed Yagi feed," *Int. J. Electron. Commun.*, vol. 1, Nov. 2019, Art. no. 152921.

[34] D. R. Smith, D. C. Vier, T. Koschny, and C. M. Soukoulis, "Electromagnetic parameter retrieval from inhomogeneous metamaterials," *Phys. Rev. E, Stat. Phys. Plasmas Fluids Relat. Interdiscip. Top.*, vol. 71, no. 3, pp. 1–11, Mar. 2005.

[35] C. G. Parazzoli, R. B. Greegor, K. Li, B. E. C. Koltenbah, and M. Tanielian, "Experimental verification and simulation of negative index of refraction using Snell's law," *Phys. Rev. Lett.*, vol. 90, no. 10, pp. 1–4, Mar. 2003.

[36] C. M. Saleh, E. Almajali, S. S. Alja'afreh, and J. Yousaf, "Dual U-slot patch antenna for 5G applications," in *Proc. IEEE Int. Symp. Antennas Propag. USNC-URSI Radio Sci. Meeting (APS/URSI)*, Dec. 2021, pp. 349–350.

[37] R. A. dos Santos, G. L. Fré, and D. H. Spadoti, "Technique for constructing hemispherical dielectric lens antennas," *Microw. Opt. Technol. Lett.*, vol. 61, no. 5, pp. 1349–1357, May 2019.

[38] A. O. Diallo, R. Czarny, B. Loiseaux, and S. Hole, "Comparison between a thin lens antenna made of structured dielectric material and conventional lens antennas, in Q-band in a compact volume," *IEEE Antennas Wireless Propag. Lett.*, vol. 17, no. 2, pp. 307–310, Feb. 2018, doi: 10.1109/LAWP.2017.2787789.

[39] H.-N. Hu, F.-P. Lai, and Y.-S. Chen, "Dual-band dual-polarized scalable antenna subarray for compact millimeter-wave 5G base stations," *IEEE Access*, vol. 8, pp. 129180–129192, 2020.

[40] E. A. Abbas, M. Ikram, A. T. Mobashsher, and A. Abbosh, "MIMO antenna system for multi-band millimeter-wave 5G and wideband 4G mobile communications," *IEEE Access*, vol. 7, pp. 181916–181923, 2019.

[41] Y. Pan, Y. Cui, and R. Li, "Investigation of a triple-band multibeam MIMO antenna for wireless access points," *IEEE Trans. Antennas Propag.*, vol. 64, no. 4, pp. 1234–1241, Apr. 2016.
[42] A. Goudarzi, M. M. Honari, and R. Mirzavand, "A millimeter-wave Fabry–Pérot cavity antenna with unidirectional beam scanning capability for 5G applications," *IEEE Trans. Antennas Propag.*, vol. 70, no. 3, pp. 1787–1796, Mar. 2022.

CHAKER MOHSEN SALEH received the B.Sc. degree in electronics and communications engineering, the master's degree in telecommunication and networks, and the Ph.D. degree in electronic systems and telecommunication from the University of Laghouat, Laghouat, Algeria, in 2010, 2012, and 2016, respectively. He is currently an Associate Professor with the Department of Electronic and the LTSS Laboratory, University of Laghouat. His research interests include smart antennas, metamaterial for 5G and 6G applications, and the application of machine learning to antennas design.

EQAB ALMAJALI (Member, IEEE) received the B.Sc. degree (Hons.) from Mu'tah University, Jordan, in 2002, and the M.A.Sc. and Ph.D. degrees (Hons.) in electrical engineering from the University of Ottawa, Ottawa, ON, Canada, in 2010 and 2014, respectively. He has been an Assistant Professor with the Electrical Engineering Department, University of Sharjah, since August 2018. Prior to that, he worked as a Postdoctoral Fellow at the Electronics Department, Carleton University, Canada. He is the author of over 50 technical publications and two book chapters. His current research interests and activities include frequency selective surfaces, millimeter-wave MIMO antennas, integrated 4G/5G antennas for wireless handsets, transmit-arrays, and low profile holographic antennas and microwave sensors. He was awarded the prestigious Canadian National Science and Engineering Research Council (NSERC) Postdoctoral Fellowship for his research excellence, in 2014, and also awarded the NSERC-PGS Scholarship during his doctoral studies in 2012.

ANWAR JARNDAL (Senior Member, IEEE) received the Ph.D. degree in electrical engineering from the University of Kassel, Kassel, Germany, in 2006. He was a Postdoctoral Fellow at the Ecole de Technologie Superieure (ETS), Quebec University, Canada. He is currently an Associate Professor with the Department of Electrical Engineering, University of Sharjah. He has published over 110 internationally peer-reviewed publications. He has many research interests include active devices modeling, measurements and characterization techniques, power amplifiers design, low-noise amplifier design, local and global optimizations, artificial neural networks, machine learning, fuzzy logic, radio channel modeling, and wireless power transfer. He is serving as a reviewer for more than 20 international journals. He received the Annual Incentives Award for the Distinguished Faculty in scientific research from the University of Sharjah. His was also classified as one of the World's Top 2% Scientists 2020 (Stanford University).

JAWAD YOUSAF received the M.S. and Ph.D. degrees in electronics and electrical engineering from Sungkyunkwan University, Suwon, South Korea, in 2016 and 2019, respectively. He worked as a prestigious Brain of Korea (BK) Postdoctoral Fellow at the EMC Laboratory, Sungkyunkwan University, from March 2019 to July 2019. Also, he worked as the Senior RF Researcher at the Pakistan Space and Upper Atmosphere Research Commission (SUPARCO: National Space Agency of Pakistan), from 2009 to 2013. He has been currently working as an Assistant Professor with the Electrical, Computer, and Biomedical Engineering Department, Abu Dhabi University, United Arab Emirates, since August 2019. His research interests include applications of artificial intelligence in electromagnetics and bio-applications, electrostatic discharge (ESD), EMI/EMC, reverberation chamber, antenna design and modeling, chipless RFID tags, and analysis of socio-economic problems. His research work has resulted in over 90 publications in leading peer-reviewed international technical journals, and refereed international and national conferences. He was a recipient of prestigious Brain of Korea (BK)-21 Postdoctoral Fellowship 2019; the 2nd Best Ph.D. Graduate Award of College 2019; the Best Paper Award in 49th KIEE Summer Conference 2018; winner of the Grand Prize for Best Paper in 3rd Electromagnetic Measurement Competition of KIESS 2018; the Prestigious Annual EMC Scholarship Award of KIEES and EMCIS Company Ltd., in 2017; the Best EMC Symposium Paper Award; and the EDCOM Best Student Paper Award Finalist, IEEE International Symposium on EMC and SI/PI 2017 (USA), in 2017.

SAQER S. ALJA'AFREH received the B.Sc.Eng. and M.Sc.Eng. degrees from the Faculty of Engineering, Mutah University, Al Karak, Jordan, in 2004 and 2007, respectively, and the Ph.D. degree in electrical engineering from the University of Liverpool, Liverpool, U.K., in November 2015. He worked as a Field Engineer at Amman, Jordan, from 2005 to 2009, and as a Lecturer at the Department of Electrical Engineering, Mutah University, from 2009 to 2012. He has been an Associate Professor with the Electrical Engineering Department, Mutah University, since November 2015. He was worked as the Head of the Electrical Engineering Department, Mutah University, from 2017 to 2018, and from 2020 to 2021. He published over 60 refereed papers in leading journals and conference proceedings. His current research interests include MIMO and diversity antennas, 4G/5G antennas, dielectric resonator antennas, planar antennas, and microwave circuits. Recently, he received a 50,000 GBP Royal Academy Grant for the development of an undergraduate industry related mobile communications course in communications engineering curriculum. He was a co-PI in other five granted research project. In summer 2018, he was awarded the Guest Visit Award of the Doutche Forschungsgemeinschaft German Research Foundation.

RONY E. AMAYA (Senior Member, IEEE) received the M.Eng. and Ph.D. degrees from Carleton University, Ottawa, ON, Canada, in 2001 and 2005, respectively. He joined the Design Center, Skyworks Solutions, Ottawa, in 2003, and involved in the design of RFIC's for wireless transceivers. He held a research scientist position at the Communications Research Centre Canada, from 2006 to 2015, developing research and developing technology for integrated RF circuit and system solutions from S-Band to E-Band and addressing packaging and antenna integration. He is currently manages research programs in collaboration with the National Research Council (NRC), KennedyLabs, Nanowave Technologies, ELPHIC and Cienna. He joined the Department of Electronics, Carleton University, as an Associate Professor, in 2016. He has authored or coauthored more than 100 technical papers in journals and conference proceedings and holds several patents. His research interests include RF system design, MMICs and packaging for high-frequency and high-speed applications, active antennas and metamaterials, and energy harvesting and wireless power transfer.